Advanced Ceramics Progress: Vol. 12, No. 2, (Spring 2026) 1-10

Materials and Energy Research Center
MERC

Contents lists available at ACERP

Advanced Ceramics Progress

Journal Homepage: www.acerp.ir

Original Research Article

Unveiling Lithium-ion Migration Mechanisms in Anti-perovskite Solid Electrolytes: A Combined EIS and EDS Study of Defect Dynamics

Abouzar Massoudi [a,*]

[a] *Associate Professor, Department of Semiconductors, Materials and Energy Research Center (MERC), P.O. Box 14155/4777, Karaj, Iran.*

* Corresponding Author Email: massoudi@merc.ac.ir (A. Massoudi) URL: https://www.acerp.ir/article_247046.html

ARTICLE INFO

Article History:

Received 07 June 2026
Revised ? 28 June 2026
Accepted 05 July 2026

Keywords:

Solid-State Batteries
Lithium-Ion Conductivity
Defect Chemistry
Ruddlesden–Popper Phases
Electrochemical Impedance Spectroscopy

ABSTRACT

Understanding the defect-mediated migration mechanisms in solid electrolytes is critical for optimizing lithium-ion conductivity. This study investigates Li^+ transport in lithium halide hydroxide anti-perovskite materials by systematically correlating defect structures with electrochemical performance. Samples with controlled compositions of $Li_2(OH)_{1-x}F_xCl$ (x=0.005) were synthesized to stabilize orthorhombic, cubic, and Ruddlesden–Popper (RP) structural phases. To investigate ion transport mechanisms and elemental shifts during thermal cycling, EIS and EDS techniques were employed. EIS analysis revealed distinct activation energies associated with specific migration mechanisms: low-temperature transport in the RP and cubic phases was governed by Li^+ vacancy or interstitial dumbbell migration, whereas high-temperature regimes were dominated by Schottky defect formation in LiCl or Li_2O. Complementary EDS findings indicated an increase in oxygen vacancies post-cycling, thereby corroborating the hypothesis regarding Schottky pair generation. Furthermore, high grain boundary resistance was attributed to excessive barriers arising from hydrogen-related defects. These findings provide a mechanistic framework for designing low-resistance solid-state electrolytes through the control of defect chemistry.

https://doi.org/10.30501/acp.2026.584755.1198

1. INTRODUCTION

The transition toward all-solid-state batteries (ASSBs) represents a pivotal advancement in energy storage technology, primarily driven by the urgent need to enhance safety, energy density, and cycle life compared to conventional lithium-ion batteries (Jaradat & Khatib, 2025; Moghadami et al., 2024; Nangir et al., 2024; Shang et al., 2025). Among various solid electrolyte candidates, hydroxide-chloride anti-perovskite solid electrolytes, particularly Li_2OHCl, have emerged as highly promising materials due to their exceptional ionic conductivity, wide electrochemical stability window, and ease of processing via wet-chemical methods (Dawson et al., 2021; Deng et al., 2022; Guo et al., 2021; Nangir et al., 2023, 2025; Ye et al., 2021; Zheng et al., 2021). Despite these advantages, the practical implementation of Li_2OHCl is significantly hindered by its thermodynamic instability and phase transition behavior. Specifically, the material undergoes a structural phase

Please cite this article as: Massoudi, A. (2026). Unveiling Lithium-ion Migration Mechanisms in Anti-perovskite Solid Electrolytes: A Combined EIS and EDS Study of Defect Dynamics. *Advanced Ceramics Progress*, *12*(2), 1-10. https://doi.org/10.30501/acp.2026.584755.1198

transition from a low-conductivity orthorhombic phase to a high-conductivity cubic phase at approximately 45 °C. This relatively low transition temperature restricts the operational stability of the high-performance cubic phase under ambient conditions, thereby limiting its applicability in conventional battery devices.

To address these intrinsic limitations, numerous approaches have been investigated to stabilize the cubic phase and enhance the thermal stability of the electrolyte through cationic and anionic doping (Koedtruad et al., 2020; Nangir et al., 2023; Sugumar et al., 2020). For instance, recent studies have demonstrated that substituting Li with Na or K can effectively stabilize the high-conductivity cubic phase at room temperature by inducing lattice strain and increasing configurational entropy (Gao et al., 2023). Similarly, cationic substitution with Mg, Ca, or Sr has been shown to enhance ionic conductivity by creating vacancies and lowering the activation energy for ion migration (Dawson et al., 2018; Yan et al., 2026). Furthermore, anionic doping with oxygen (O) or sulfur (S) has been investigated to tune the electrochemical stability window and improve interfacial compatibility with electrode materials (Luo et al., 2024; Qian et al., 2026).

In 2014, Braga and colleagues demonstrated the synthesis of the glass-ceramic $Li_{3-2x}Ba_xOCl$ (where $x = 0.005$), which exhibited an exceptionally high ionic conductivity of 22.5×10^{-2} S cm^{-1} at room temperature (25 °C). According to the methodology reported in (Braga et al., 2014), the electrolyte was fabricated by co-heating lithium hydroxide, lithium chloride, and barium hydroxide with minimal water addition in a Teflon reactor at 220-240 °C. To obtain a dry crystalline intermediate, the system was heated and subsequently evacuated. The final glassy material was produced by annealing this intermediate in air. Contrary to the initial reports, Hangehofer et al. identified the crystalline product as a dual-phase mixture consisting of $Li_{1.84}H_{1.16}OCl$ and $Li_4(OH)_3Cl$. Furthermore, their analysis indicated that air-heating this mixture leads to the formation of $LiCl{\cdot}xH_2O$, which possesses significantly high electrical conductivity (Hanghofer et al., 2018). While previous studies have focused on metal cation substitutions, the role of anionic doping, particularly with fluorine (F), remains a critical yet underexplored avenue for structural engineering. Fluorine, being highly electronegative and having a smaller ionic radius than chlorine and oxygen, is expected to induce significant lattice distortion and local disorder, potentially lowering the energy barrier for phase transitions and enhancing ionic mobility (Li et al., 2016).

Understanding the degradation mechanisms in hydroxide-chloride solid-state electrolytes requires a thorough examination of their defect chemistry, particularly the role of anionic vacancies and interfacial impurities. Recent studies have highlighted that electrochemical cycling induces significant structural changes that are not immediately apparent through bulk conductivity measurements alone. Specifically, complementary EDS analyses revealed an increase in oxygen vacancies post-cycling, a finding that provides critical microstructural evidence for the Schottky pair formation hypothesis. This hypothesis suggests that the loss of oxygen ions from the lattice is compensated by the creation of corresponding cationic vacancies to maintain charge neutrality. As noted by Braga and later corroborated by Hangehofer, the formation of these Schottky pairs is not merely a theoretical construct but a tangible consequence of cycling, leading to local lattice relaxation and potential structural instability.

However, the impact of these bulk defects extends beyond the crystal lattice, significantly influencing interfacial properties. A major challenge in optimizing the performance of these electrolytes is the high grain boundary resistance, which often limits overall ionic conductivity. Recent literature attributes this resistance not only to conventional space-charge effects but also to additional barriers arising from hydrogen-related defects. Given the hygroscopic nature of hydroxide-based materials, hydrogen species tend to segregate at grain boundaries, forming insulating layers or creating complex defect landscapes that impede lithium-ion transport. This segregation is exacerbated by the presence of oxygen vacancies, which can alter the local chemical environment and promote hydrogen trapping (Braga et al., 2013; Lu et al., 2015; Nangir et al., 2024, 2025; Stegmaier et al., 2017; Yin et al., 2020).

The interplay between oxygen vacancies and hydrogen-related defects creates a synergistic effect that degrades electrochemical performance. While Schottky defect formation explains the bulk structural changes, the accumulation of hydrogen at grain boundaries accounts for the interfacial bottlenecks. This dual mechanism highlights the need for advanced characterization techniques, such as EDS and impedance spectroscopy, to decouple bulk and interfacial contributions to resistance. By addressing these specific defect pathways, future research can focus on mitigating hydrogen segregation and stabilizing the lattice against Schottky pair formation, thereby enhancing the long-term stability and conductivity of halide-hydroxide anti-perovskite solid electrolytes.

In this study, we investigate the effect of fluorine doping on the structural, thermal, and ionic properties of Li_2OHCl. By systematically substituting F, we aim to shift the orthorhombic-to-cubic phase transition to higher temperatures, thereby stabilizing the high-conductivity phase under ambient conditions. Furthermore, we analyze changes in glass transition temperature (T_g) and melting behavior to elucidate the underlying mechanisms of disorder-induced conductivity enhancement. This work provides a comprehensive understanding of the effects of anionic doping in hydroxide-chloride anti-

perovskite electrolytes, offering a viable pathway for optimizing the thermal stability and ionic performance of next-generation solid-state batteries.

2. MATERIALS AND METHODS

2.1. Solid-State Synthesis

The $Li_2(OH)_{1-x}F_xCl$ solid electrolyte was prepared using a standard solid-state reaction method. Stoichiometric quantities of lithium chloride ("LiCl", Iran, ≥99%), lithium hydroxide ("LiOH", Germany, ≥99%), and lithium fluoride ("LiF", Germany, ≥99%) were precisely weighed at molar ratios of 1:2:0.005, respectively. To ensure a homogeneous mixture, the precursor components were thoroughly ground using an agate mortar and pestle. The resulting powder was then placed in a 316L stainless-steel crucible and annealed in a vacuum furnace at 240 °C for 48 h. The heating rate was maintained at $5°C\ min^{-1}$, followed by natural cooling to room temperature.

2.2. Material Characterization

2.2.1. Structural and Morphological Analysis

The crystallographic structure and phase purity were evaluated via X-ray diffraction (XRD) using a Philips PW 3710 diffractometer (Germany) with Cu Kα radiation (λ = 1.5405 Å). Diffraction patterns were recorded over a 2θ range of 5° to 80° with a step size of 0.02°. The microstructural characteristics and elemental distribution of the samples were investigated using a Zeiss Sigma VP scanning electron microscope (SEM) integrated with an energy-dispersive X-ray spectroscopy (EDS) system. Thermal stability was assessed via differential scanning calorimetry (DSC) using a METTLER instrument. These measurements were conducted under a nitrogen atmosphere (50 mL min^{-1} flow rate) with a controlled heating rate of 5 °C min^{-1}. Additionally, the chemical bonding and functional groups were analyzed using Fourier transform infrared spectroscopy (FTIR) on a Spectrum 400 instrument over the spectral range of 4000–400 cm^{-1}.

2.2.2. Electrochemical Impedance Spectroscopy (EIS)

For electrochemical measurements, the synthesized powder was uniaxially pressed at 3000 bar to form dense pellets with a thickness of approximately 1 mm. To investigate the bulk and grain boundary conductivity, symmetric cells were assembled using gold (Au) blocking electrodes on both sides of the pellet. Impedance spectroscopy measurements were performed using an EG&G Parstat 2273 potentiostat/galvanostat over a frequency range of 100 "mHz" to 1 "MHz" with an AC amplitude of 10 "mV" (rms). The temperature-dependent impedance data were collected using a temperature-controlled chamber (A. Kaem MOD TU16, 5 A, 250 V) under controlled heating and natural cooling conditions.

3. RESULTS AND DISCUSSION

3.1. Structural Characterization and Phase Analysis

Figure 1a presents the XRD pattern of the synthesized $Li_2(OH)_{0.995}F_{0.005}Cl$. The diffraction peaks are primarily indexed to a cubic lattice with $Pm\bar{3}m$ symmetry, characteristic of the pure Li_3OCl phase, with a spiky peak observed at $2\theta = 32.22°$. However, the presence of secondary phases is evident, specifically orthorhombic Li_2OHCl (*Pban* symmetry) with a compressed lattice volume of $230\ Å^3$, and $Li_4(OH)_3Cl$ with a lattice volume of $242\ Å^3$.

The atomic coordination analysis reveals significant structural rearrangements induced by fluorine doping. In the Li_2OHCl structure, lithium ions initially located at the 3d positions redistribute to the 4a and 4c sites, while hydrogen (H1) occupies the 16h sites. This redistribution leads to statistical distortion within the lattice. The calculated bond lengths for O-H1 and O2-H2 are 0.945 "A" ˚ and 0.788 "A" ˚, respectively. The incorporation of fluorine, which possesses higher electronegativity and greater negative charge density than the host anions, likely shortens the O-H bond distances, thereby reducing the overall lattice parameter. This interplay between lattice expansion and compaction induces slight distortions in the octahedral Li_6O coordination environment.

To evaluate the structural stability, the Goldschmidt tolerance factor (t) was calculated. For a general perovskite-like structure M_3BA, t is defined as: $t = \frac{r_B + r_M}{\sqrt{2}(r_A + r_M)}$ where r_A, r_B, and r_M represent the ionic radii of the A-site anion (e.g., Cl, Br), B-site anion (e.g., O, OH), and M-site cation, respectively. Ideally, $t = 1$ corresponds to a perfect cubic structure. Deviations from unity indicate potential phase instability, octahedral tilting, or ionic mismatch. Specifically, $t > 1$ may promote face-sharing of $[M_3B]$ octahedra to accommodate larger A-site ions, whereas $t < 1$ favors octahedral tilting to stabilize smaller A-site ions [19]. For the Li_2OHCl constitution, the calculated tolerance factor is $t = 0.71$. This value is far from unity, suggesting tilting and instability. For the $Li_2(OH)_{0.995}F_{0.005}Cl$ constitution, the calculated tolerance factor is $t = 0.90$. This value, being close to unity, suggests a relatively regular and highly symmetric structure, consistent with the dominant cubic phase observed in the XRD pattern.

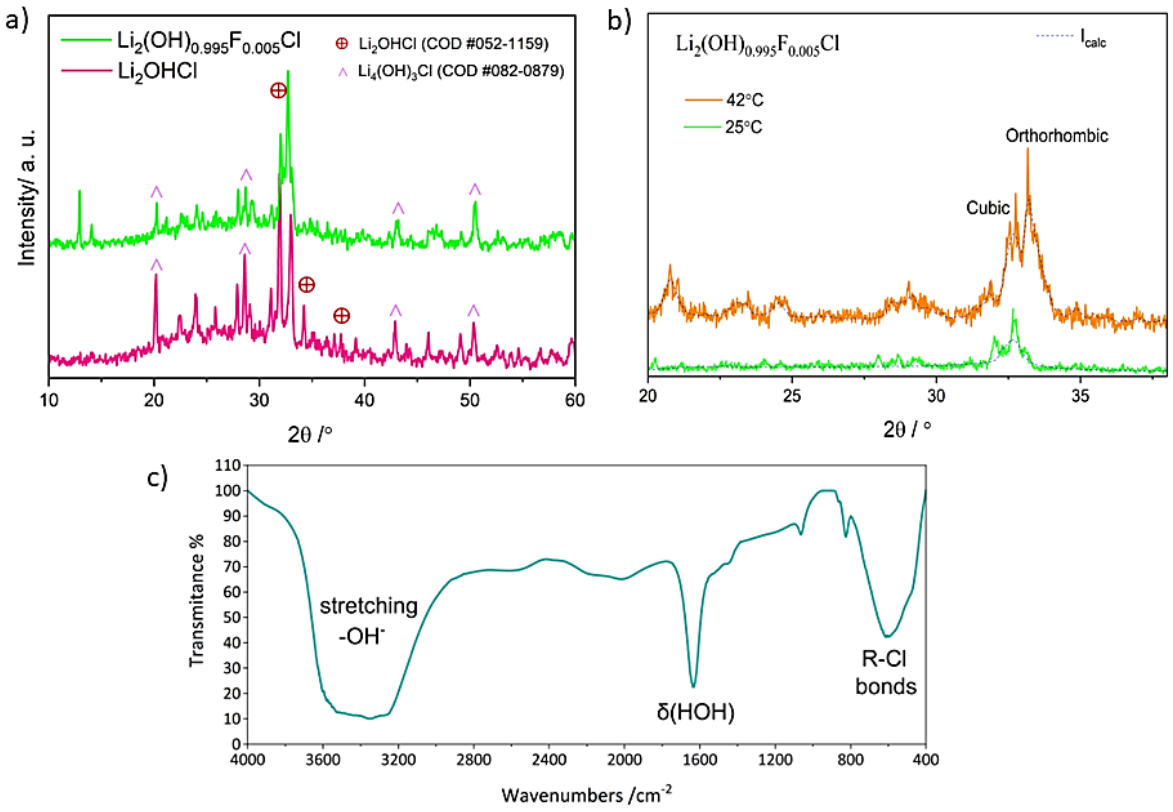

Figure 1. a) The XRD patterns of undoped and F-doped Li_2OHCl; b) The XRD patterns of F-doped Li_2OHCl at room temperature and elevated temperature; c) FTIR plot.

3.2. Vibrational Spectroscopy Analysis

The local bonding environment and functional groups in $Li_2(OH)_{0.995}F_{0.005}Cl$ were investigated via FTIR spectroscopy, as depicted in Figure 1b. The broad absorption band in the range of 3200–3632 cm^{-1} is related to the stretching vibrations of OH^- groups, indicating the presence of both free hydroxide ions and hydrogen-bonded species. A spiky peak at 1645 cm^{-1} corresponds to the bending vibration (δ_{HOH}) of residual water content. Furthermore, distinct peaks at 586 cm^{-1} and 826 cm^{-1} are liked to halogen-related vibrations, specifically indicative of R-Cl bonds and metal-halide lattice modes [20]. These spectral features corroborate the coexistence of hydroxide and halide species within the crystal lattice, supporting the complex phase composition identified by XRD.

3.3. Thermal Analysis

DSC analysis (25–350 °C, 5 °C min^{-1}, N_2) reveals that F-doping shifts the orthorhombic-to-cubic phase transition of Li_2OHCl from 42–45 °C to 70°C, a change corroborated by HT-XRD (Fig. 1-b). This multivalent doping also lowers the glass transition temperature (T_g) from 129 °C (Li_2OHCl) to 109 °C ($Li_2(OH)_{0.995}F_{0.005}Cl$), evidenced by DSC baseline perturbations and broad XRD plateaus (20–30°). While undoped Li_2OHCl melts sharply at 291°C, $Li_2(OH)_{0.995}F_{0.005}Cl$ exhibits a split melting profile: a lower-temperature endotherm (T ≈ 272 °C) indicating local disordering and a higher-temperature peak (T ≈ 284 °C) representing bulk melting. The resulting ΔT reflects lattice mismatch between local and bulk structures. An additional endotherm at 224 °C in $Li_2(OH)_{0.995}F_{0.005}Cl$ signifies a crystalline-to-amorphous transition in hydride/hydroxide sublattices. During cooling, nucleation and crystallization occur at reduced temperatures compared to the pure sample, attributed to the accelerated onset of the glassy transition induced by larger dopant atoms.

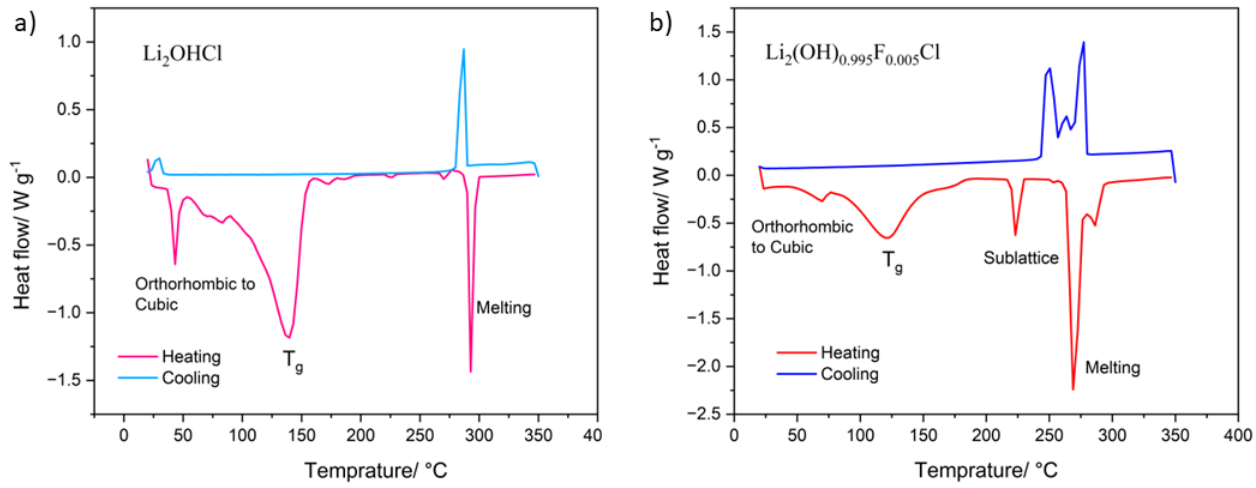

Figure 2. DSC curves of a) undoped Li_2OHCl and b) F-doped Li_2OHCl.

3.4. Electrochemical Impedance Spectroscopy (EIS) Analysis

Figure 2 presents the Nyquist plots obtained from EIS measurements for the $Li_2(OH)_{0.995}F_{0.005}Cl$ electrolyte. The impedance spectra were fitted using an equivalent circuit model consisting of an ohmic resistance (R_s) in series with two parallel (RQ) elements. The first (RQ) element represents the combined resistance of the grain and grain boundary (R_{g+gb}), while the second element, characterized by a Constant Phase Element (CPE), models the dielectric properties of the solid-state electrolyte within the charge-space layer [21]. The ion conductivity (σ_i) was calculated using the following equation:

$$\sigma_i = \frac{d}{R_i A} \quad (1)$$

where d is the thickness of the pellet, A is the electrode area, and R_i represents the total bulk resistance, determined by the high-frequency intercept on the real axis of the Nyquist plot.

The temperature-dependent ionic conductivity was monitored during both heating and cooling cycles. In the symmetric blocking Au || Au cell, solid Li_2OHCl pellet yields ion conductivity values: 2×10^{-4} S cm^{-1} at 25°C and 5.5×10^{-3} S cm^{-1} at 60 °C. The ionic conductivity in the bulk at room temperature is twice the value at the grain boundary, i.e., 1.17×10^{-4} S cm^{-1}. When the transition from orthorhombic to cubic phase occurs, a jump in ionic conductivity is observed, and σ_{gb} reaches 3.1×10^{-3} S cm^{-1} at 60 °C.

In a symmetric Au||Au cell, substituting F^- for the anion OH^- stabilizes the more desirable anti-perovskite structure, resulting in higher lithium-ion conductivity. The ion conductivity in the grains (2.6×10^{-4} S cm^{-1}) is comparable to that at the grain boundaries (2.8×10^{-4} S cm^{-1}) at room temperature, and both values significantly surpass the relatively weak conductivity of the undoped Li_2OHCl sample. In many solid electrolytes, grain boundaries act as major bottlenecks (high resistance) for ion transport. The fact that $Li_2(OH)_{0.995}F_{0.005}Cl$ shows comparable values suggests that F^- doping effectively eliminates or reduces the grain boundary resistance barrier, making the entire material more uniformly conductive. Anionic impurities with smaller ionic radii, such as F^-, facilitate lithium-ion migration within the anti-perovskite framework by inducing rotational disorder in the local coordination environment. Furthermore, the high electron affinity of F^-, due to its high electronegativity, provides a plausible explanation for the easier movement of lithium ions throughout the sample. For a lithium ion to jump more easily into vacancy, it requires a driving force to orient its motion. Consequently, the electronegative character of the doped fluorine ions directs the movement of lithium ions toward the interface. Otherwards, replacing the larger/hydrogen-bonding OH^- anion with the smaller F^- anion stabilizes the anti-perovskite crystal structure. This stabilization leads to a material with significantly more ion conductivity compared to the undoped. Moreover, The smaller size of F^- compared to OH^- creates space and induces "rotational disorder" in the local coordination environment. This disorder likely creates more open pathways or lowers the energy barrier for lithium ions to move through the lattice, facilitating migration.

3.5. Defect Chemistry and Morphological Evolution

The activation energy (E_a) for ionic conduction was calculated based on the Arrhenius plot of the ionic conductivity. For the symmetric Au || Li_2OHCl || Au cell, the E_a values were determined to be 0.24 eV during the heating cycle. These values

suggest that the migration mechanism is governed by vacancy V'_{Li}. For the symmetric Au || $Li_2(OH)_{0.995}F_{0.005}Cl$ || Au cell, the E_a values were determined to be 1.68 eV during the heating cycle. These values suggest that the migration mechanism is governed by Schottky defects associated with the Li_2O sublattice.

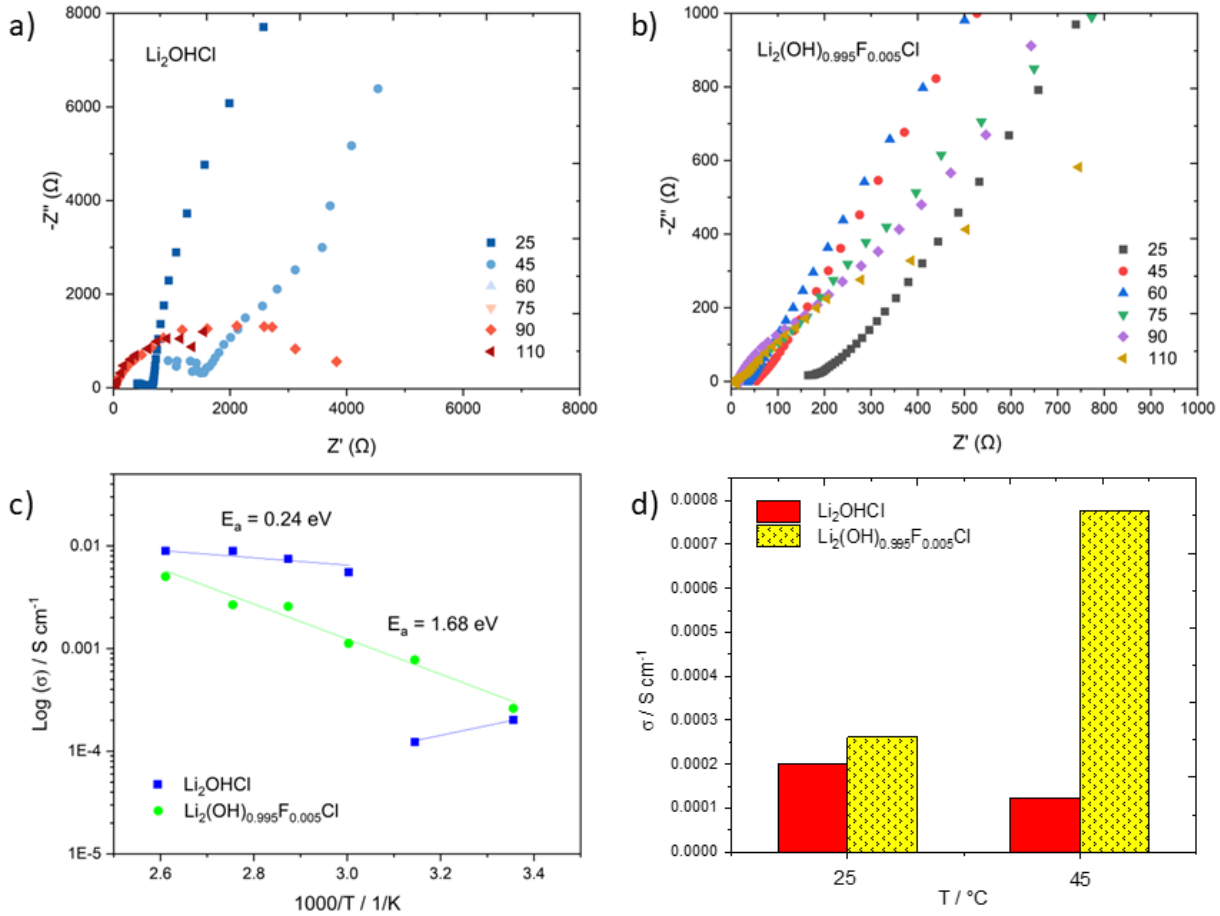

Figure 3. (a–b) Nyquist curves from symmetric Au-electrode cells; (c) Arrhenius plots ($log\ \sigma$ vs. $1/T$) indicating the activation energy; (d) Bar graph comparing the ionic conductivity of undoped versus F-doped Li2OHCl.

As is well known, in many ceramic electrolytes, grain boundaries act as high-resistance barriers that impede ion flow. The data in Figure 3d indicate that F^- doping effectively removes this barrier, allowing ions to move freely across both regions. The bulk ionic conductivity at 45 °C in $Li_2(OH)_{0.995}F_{0.005}Cl$ is approximately six times higher than that of Li_2OHCl.

Figure 4 illustrate the surface morphology of $Li_2(OH)_{0.995}F_{0.005}Cl$ and Li_2OHCl pellets before and after EIS measurements. Prior to testing, the pellets exhibited smooth, dense surfaces with well-defined grain boundaries. However, post-EIS analysis revealed significant morphological changes: the surfaces became distorted, exhibiting swelling, pore formation, and the development of fissures and wrinkles. The initially smooth surfaces were characterized by a high density of defects after testing. Notably, the free spaces appeared saturated with a molten phase, and surface nucleation indicated the formation of new structural phases. Specifically, the growth of internal anti-perovskite layers alongside rock-salt-like structures resembled a two-dimensional Ruddlesden–Popper (RP) phase, a phenomenon previously reported in similar halide hydroxides (Zhao et al., 2021). Such rock-salt-like features were absent on the grain surfaces before the EIS test, suggesting that electrochemical polarization induces phase segregation or local restructuring.

Elemental analysis via EDS in Figure 5 provides further insight into the compositional changes. Before EIS, the sample contained 1.9 wt% F, 11.9 wt% O, and 86.1 wt% Cl. The high chlorine content indicates a Cl-rich composition. By converting the measured weight percentages into molar ratios based on atomic weights (Cl: 35.45 g/mol, O: 16.00 g/mol), we determined a Cl-to-O ratio of approximately 2.42:0.74. This significant deviation from the ideal stoichiometry of

$Li_2(OH)_{0.995}F_{0.005}$ suggests the formation of a highly defective anti-perovskite lattice. Such disorder is characteristic of solid-state superionic conductors, where incomplete occupancy of crystallographic sites creates high defect concentrations. Although perfectly ordered Li_3OCl is theoretically predicted to exhibit poor conductivity, disordered halide hydroxides such as Li_2OHCl maintain charge neutrality through mobile defect carriers.

The defect chemistry can be described using Kröger-Vink notation. The relevant reactions include:

1. LiCl Schottky Pair Formation: $Li_{Li}^{\times} + Cl_{Cl}^{\times} \rightleftharpoons V_{Li}' + V_{Cl}^{\cdot} + LiCl$ This leads to the formation of $Li_{3-x}OCl_{1-x}$.
2. Li_2O Schottky Pair Formation: $2Li_{Li}^{\times} + O_O^{\times} \rightleftharpoons 2V_{Li}' + V_O^{\cdot\cdot} + Li_2O$ This results in $Li_{3-2x}O_{1-x}Cl$.
3. Li_2O Substitution by Cl: $Li_2O + Cl_{Cl}^{\times} \rightleftharpoons O_{Cl}' + Li_i^{\cdot} + LiCl$ This produces $Li_{3+x}O_{1+x}Cl_{1-x}$.
4. Frenkel Defect Formation: $Li_{Li}^{\times} \rightleftharpoons V_{Li}' + Li_i^{\cdot}$.

Literature values for defect formation energies vary. Wu evaluated the Schottky formation energies for Li_2O and LiCl to be 1.54 "eV" and 1.27 "eV", respectively (Wu et al., 2018), whereas Braga reported a higher value of 4.75 "eV" for the "LiCl" Schottky defect (Braga et al., 2013). The experimentally derived E_a of ~ 1.68 eV (Fig. 3c) aligns closely with the Li_2O Schottky defect energy, suggesting that this defect type dominates the conduction mechanism. This is further supported by the possibility of an interstitial dumbbell mechanism with a lower barrier (0.15-0.18 "eV") (Hanghofer et al., 2018), although the higher experimental E_a indicates that vacancy-mediated transport is the dominant pathway.

Post-EIS EDS analysis reveals a significant shift in composition: the F content increased to 10.3 wt%, the O content decreased to 6.1 wt%, and the Cl content changed to 83.6 wt%. The decrease in oxygen content and the corresponding increase in fluorine suggest an enrichment of oxygen vacancies ($V_O^{\cdot\cdot}$) in the structure. This supports the formation of Li_2O Schottky pairs ($2V_{Li}' + V_O^{\cdot\cdot}$). Furthermore, recent studies by Zhao indicate that Li^+ interstitial migration along the edges of Li_6O octahedra follows a two-dimensional Ruddlesden–Popper (RP) phase pathway with a low energy barrier of 0.17 eV (Zhao et al., 2021). The morphological evolution observed in Fig. 4, resembling RP structures, corroborates this low-barrier migration mechanism in the modified surface layers.

Complementary energy-dispersive X-ray spectroscopy (EDS) analysis provided critical microstructural evidence supporting the formation of Schottky defect pairs during electrochemical cycling. Specifically, the data revealed a statistically significant increase in oxygen vacancy concentration in the cycled samples compared to their pristine counterparts. This accumulation of anionic vacancies is consistent with the Schottky pair formation hypothesis, wherein the loss of oxygen ions from the lattice is compensated by the creation of corresponding cationic vacancies to maintain charge neutrality. The presence of these vacancies facilitates local lattice relaxation and may contribute to the observed degradation in structural integrity over extended cycling periods.

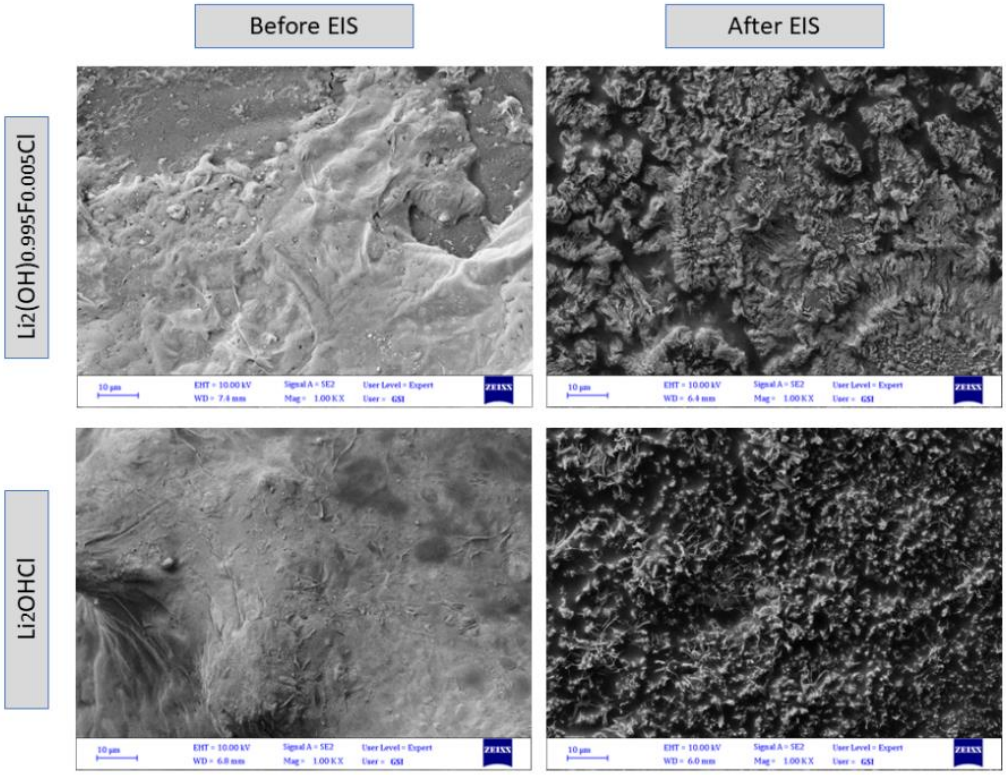

Figure 4. SEM images of undoped and F-doped Li_2OHCl pellets in different conditions.

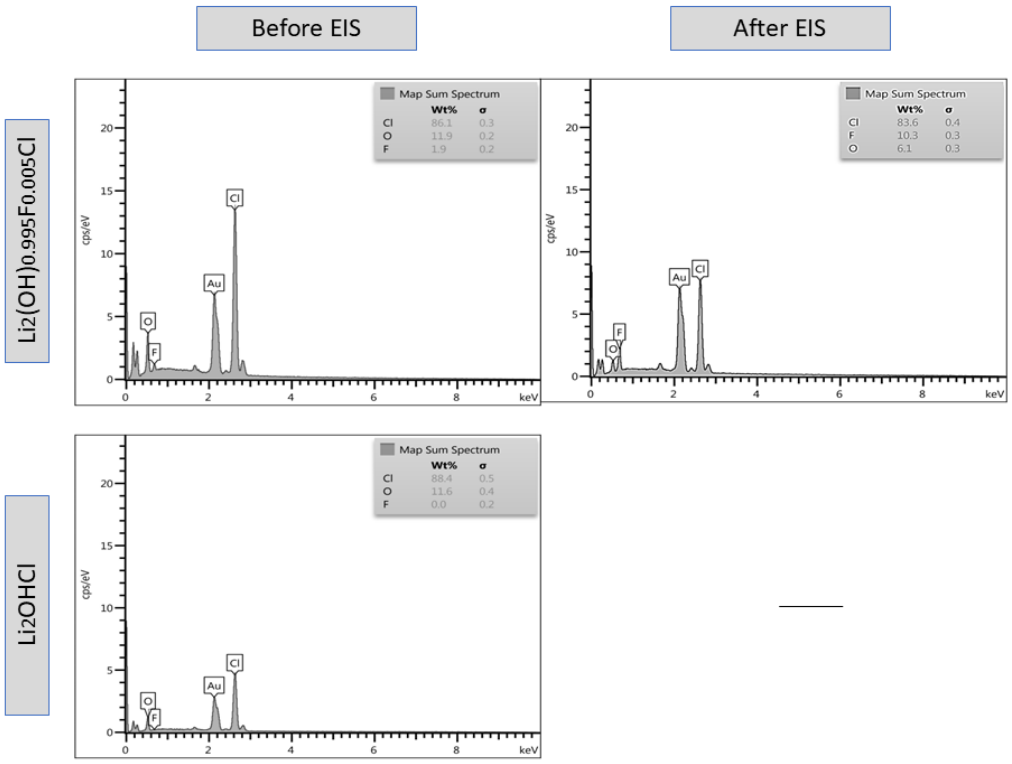

Figure 5. EDS results of undoped and F-doped Li_2OHCl.pellets in different conditions.

Furthermore, the impedance spectroscopy results highlighted a pronounced increase in grain boundary resistance, which was not solely attributable to standard interfacial effects. Detailed analysis suggests that this additional resistance arises from specific barriers induced by hydrogen-related defects. Given the hygroscopic nature of hydroxide-chloride anti-perovskite solid electrolytes, hydrogen species, likely in the form of protons or hydroxyl groups, tend to segregate at grain boundaries during processing and cycling. These hydrogen-rich phases can act as insulating layers or create space-charge regions that impede lithium-ion transport across grain boundaries. Consequently, the interplay between oxygen vacancies and hydrogen segregation creates a complex defect landscape that significantly limits the overall ionic conductivity and electrochemical performance of the material.

4. CONCLUSIONS

This study demonstrates that fluorine (F) doping significantly improves the thermal and structural stability of the Li_2OHCl solid electrolyte. Fluorine doping shifts the orthorhombic-to-cubic phase transition from 45 °C to 70 °C, thereby stabilizing the highly conductive cubic phase over a broader temperature range. Concurrently, the reduction in the glass transition temperature (T_g) from 129 °C to 109 °C and the emergence of a split melting profile indicate induced local disorder and lattice mismatch. These structural modifications, corroborated by HT-XRD and thermal analysis, facilitate enhanced ionic properties and thermodynamic stability. Ultimately, this work establishes precise structural engineering through fluorine doping as a viable strategy for overcoming thermal limitations in hydroxide-chloride solid electrolytes.

ACKNOWLEDGEMENTS

This project was supported by Materials and Energy Research Center (MERC), Tehran, Iran (grant number 481401052).

REFERENCES

1. Braga, M., Ferreira, J. A., Stockhausen, V., Oliveira, J., & El-Azab, A. (2014). Novel Li 3 ClO based glasses with superionic properties for lithium batteries. *Journal of Materials Chemistry A*, *2*(15), 5470-5480. https://doi.org/10.1039/c3ta15087a

2. Braga, M. H., Stockhausen, V., Oliveira, J. C., & Ferreira, J. A. (2013). The role of defects in Li3ClO solid electrolyte: Calculations and experiments. *MRS Online Proceedings Library*, *1526*(1), 1-5. https://doi.org/10.1557/opl.2013.519

3. Dawson, J., Famprikis, T., & Johnston, K. E. (2021). Anti-perovskites for solid-state batteries: recent developments, current challenges and future prospects. *Journal of Materials Chemistry A*, *9*, 18746-18772. https://doi.org/10.1039/D1TA03680G

4. Dawson, J. A., Chen, H., & Islam, M. S. (2018). Composition screening of lithium-and sodium-rich anti-perovskites for fast-conducting solid electrolytes. *The Journal of Physical Chemistry C*, *122*(42), 23978-23984. https://doi.org/10.1021/acs.jpcc.8b08208

5. Deng, Z., Ni, D., Chen, D., Bian, Y., Li, S., Wang, Z., & Zhao, Y. (2022). Anti-perovskite materials for energy storage batteries. *InfoMat*, *4*(2), e12252. https://doi.org/10.1002/inf2.12252

6. Gao, L., Zhang, X., Zhu, J., Han, S., Zhang, H., Wang, L., Zhao, R., Gao, S., Li, S., & Wang, Y. (2023). Boosting lithium ion conductivity of antiperovskite solid electrolyte by potassium ions substitution for cation clusters. *Nature Communications*, *14*(1), 6807. https://doi.org/10.1038/s41467-023-42385-1

7. Guo, L., Xin, C., Gao, J., Zhu, J., Hu, Y., Zhang, Y., Li, J., Fan, X., Li, Y., & Li, H. (2021). The electrolysis of anti-perovskite Li2OHCl for prelithiation of high-energy-density batteries. *Angewandte Chemie*, *133*(23), 13123-13130. https://doi.org/10.1002/anie.202102605

8. Hanghofer, I., Redhammer, G. J., Rohde, S., Hanzu, I., Senyshyn, A., Wilkening, H. M. R., & Rettenwander, D. (2018). Untangling the Structure and Dynamics of Lithium-Rich Anti-Perovskites Envisaged as Solid Electrolytes for Batteries. *Chemistry of materials*, *30*(22), 8134-8144. https://doi.org/10.1021/acs.chemmater.8b02568

9. Jaradat, T. e., & Khatib, T. (2025). A review of battery energy storage system for renewable energy penetration in electrical power system: Environmental impact, sizing methods, market features, and policy frameworks. *Future Batteries*, *7*, 100106. https://doi.org/10.1016/j.fub.2025.100106

10. Koedtruad, A., Patino, M. A., Ichikawa, N., Kan, D., & Shimakawa, Y. (2020). Crystal structures and ionic conductivity in Li2OHX (X= Cl, Br) antiperovskites. *Journal of Solid State Chemistry*, *286*, 121263. https://doi.org/10.1016/j.jssc.2020.121263

11. Li, Y., Zhou, W., Xin, S., Li, S., Zhu, J., Lü, X., Cui, Z., Jia, Q., Zhou, J., & Zhao, Y. (2016). Fluorine-doped antiperovskite electrolyte for all-solid-state lithium-ion batteries. *Angewandte Chemie International Edition*, *55*(34), 9965-9968. https://doi.org/10.1002/anie.201604554

12. Lu, Z., Chen, C., Baiyee, Z. M., Chen, X., Niu, C., & Ciucci, F. (2015). Defect chemistry and lithium transport in Li3OCl anti-perovskite superionic conductors. *Physical Chemistry Chemical Physics*, *17*(48), 32547-32555. https://doi.org/10.1039/c5cp05722a

13. Luo, Q., Liu, C., Li, L., Jiang, Z., Yang, J., Chen, S., Chen, X., Zhang, L., Cheng, S., & Yu, C. (2024). O-doping strategy enabling enhanced chemical/electrochemical stability of Li3InCl6 for superior solid-state battery performance. *Journal of Energy Chemistry*, *99*, 484-494. https://doi.org/10.1016/j.jechem.2024.07.058

14. Moghadami, M., Massoudi, A., & Nangir, M. (2024). Unveiling the recent advances in micro-electrode materials and configurations for sodium-ion micro-batteries. *Journal of Materials Chemistry A*. https://doi.org/10.1039/D4TA02096K

15. Nangir, M., Massoudi, A., & Omidvar, H. (2023). Super Ionic Li3-2xMx(OH)1-yNyCl (M=Ca, W, N=F) Halide Hydroxide as an Anti-Perovskite Electrolyte for Solid-State Batteries. *Journal of The Electrochemical Society*, *170*, 089001. http://iopscience.iop.org/article/10.1149/1945-7111/acdcbd

16. Nangir, M., Massoudi, A., & Omidvar, H. (2024). Role of hybrid solid state interface as a scavenger for anomalous Li dendrites in the lithium metal battery. *Journal of Energy Storage*, *99*, 113360. https://doi.org/10.1016/j.est.2024.113360

17. Nangir, M., Massoudi, A., & Omidvar, H. (2025). Surface modification of lithium metal anode using polar polymer-in-ceramic electrolytes by grafting of anti-perovskite for inhibition dendrite growth. *Journal of Energy Storage*, *107*, 114984. https://doi.org/10.1016/j.est.2024.114984

18. Qian, L., Ye, Y., Chen, D., Ni, D., Lin, H., Wang, X., Wu, L., Han, S., Zhu, J., & Zhao, Y. (2026). Sulfur-Doped Li2OHCl Antiperovskite Electrolyte for Stabilizing the Solid Electrolyte Interphase in Solid-State Lithium-Metal Batteries. *ACS Energy Letters*. https://doi.org/10.1021/acsenergylett.6c00619.s001

19. Shang, R., Nelson, T., Nguyen, T. V., Nelson, C., Antony, H., Abaoag, B., Ozkan, M., & Ozkan, C. S. (2025). A Comprehensive Review of Solid-State Lithium Batteries: Fast Charging Characteristics and In-Operando Diagnostics. *Nano Energy*, 111232. https://doi.org/10.1016/j.nanoen.2025.111232

20. Stegmaier, S., Voss, J., Reuter, K., & Luntz, A. C. (2017). Li+ defects in a solid-state Li ion battery: theoretical insights with a Li3OCl electrolyte. *Chemistry of materials*, *29*(10), 4330-4340. https://doi.org/10.1021/acs.chemmater.7b00659

21. Sugumar, M. K., Yamamoto, T., Motoyama, M., & Iriyama, Y. (2020). Room temperature synthesis of anti-perovskite structured Li2OHBr. *Solid State Ionics*, *349*, 115298. https://doi.org/10.1016/j.ssi.2020.115298

22. Wu, M., Xu, B., Lei, X., Huang, K., & Ouyang, C. (2018). Bulk properties and transport mechanisms of a solid state antiperovskite Li-ion conductor Li 3 OCl: insights from first principles calculations. *Journal of Materials Chemistry A*, *6*(3), 1150-1160. https://doi.org/10.1039/c7ta08780b

23. Yan, Y., Zhang, S., Man, X., Li, Q., Xue, H., Xiao, P., Shi, Y., Yin, L., & Wang, R. (2026). Emerging inorganic amorphous solid-state electrolytes in all-solid-state lithium batteries: From crystallographic order to atomic and lattice disorder. *eScience*, 100531.

24. Ye, Y., Deng, Z., Gao, L., Niu, K., Zhao, R., Bian, J., Li, S., Lin, H., Zhu, J., & Zhao, Y. (2021). Lithium-Rich Anti-perovskite Li2OHBr-Based Polymer Electrolytes Enabling an Improved Interfacial Stability with a Three-Dimensional-Structured Lithium Metal Anode in All-Solid-State Batteries. *ACS applied materials & interfaces*, *13*(24), 28108-28117. https://doi.org/10.1021/acsami.1c04514

25. Yin, L., Yuan, H., Kong, L., Lu, Z., & Zhao, Y. (2020). Engineering Frenkel defects of anti-perovskite solid-state electrolytes and their applications in all-solid-state lithium-ion batteries. *Chemical Communications*, *56*(8), 1251-1254. https://doi.org/10.1039/c9cc08382k

26. Zhao, S., Chen, C., Li, H., & Zhang, W. (2021). Theoretical insights into the diffusion mechanism of alkali ions in Ruddlesden–Popper antiperovskites. *New Journal of Chemistry*, *45*(9), 4219-4226. https://doi.org/10.1039/d0nj04850j

27. Zheng, J., Perry, B., & Wu, Y. (2021). Antiperovskite superionic conductors: a critical review. *ACS Materials Au*, *1*(2), 92-106. https://doi.org/10.1021/acsmaterialsau.1c00026